IEEE Access
Multidisciplinary | Rapid Review | Open Access Journal

Received 3 December 2022, accepted 3 January 2023, date of publication 5 January 2023, date of current version 11 January 2023.

Digital Object Identifier 10.1109/ACCESS.2023.3234762

RESEARCH ARTICLE

IRS-Aided Wireless Communication: From Physics to Channel Modeling and Characterization

VAN PHU TUAN[1] AND IC PYO HONG[2], (Member, IEEE)
[1]Faculty of Electrical and Electronics Engineering, Dong-A University, Da Nang 550000, Vietnam
[2]Department of Smart Information and Technology Engineering, Kongju National University, Cheonan 31080, South Korea

Corresponding author: Ic Pyo Hong (iphong@kongju.ac.kr)

This work was supported in part by the Basic Science Research Program under Grant 2020R1I1A3057142, in part by the Priority Research Center Program through the National Research Foundation under Grant 2019R1A6A1A03032988, and in part by the Underground City of the Future Program through the Ministry of Science and ICT.

ABSTRACT Intelligent reflecting surface has recently emerged as a cost-effective solution to overcome the deep fading and uncontrollable wireless environment. This leads to a need for studies on the wireless channels of IRS-aided wireless communication (IRSaWC). This paper proposes a novel channel modelling method for the IRSaWC by exploiting the physics characteristic of the electromagnetic (EM) field on the IRS and the modified Saleh-Valenzuela (SV) model. Firstly, the reflection on a single reflecting tile (RT) of the IRS is investigated in the presence of a misalignment between the RT's configured incident angle and the actual incident angle, and the RT's phase distortion. Then, the path loss and phase shift models for the reflected field are developed. Extending our study to the multiple-RT scenario and utilizing the modified SV model, the channel characteristic for the IRSaWC is determined. Our analysis shows that the information signal at the receiver experiences a Rice fading with controllable parameters. Theoretical results for the path loss, the channel's parameters, and the received distortion power are derived; moreover, an approximate distribution for the combined signal-to-noise ratio (SNR) for IRS-aided multiple-antenna wireless systems (IRSaMAWSs) has been investigated with the aim of conducting further studies on theoretical performance for IRSaMAWSs

INDEX TERMS Intelligent reflecting surface, channel modeling, Rice distribution, multiple-antenna system, performance analysis.

I. INTRODUCTION

The conventional wireless systems frequently operate in an uncertain wireless environment where the line-of-sight (LoS) link is commonly unavailable due to obstacles and the signals travel on multiple paths differing in time and angle before reaching the receiver. Consequently, the wireless systems may meet some issues of low reliable transmission, larger energy consumption, high latency, etc.. Recently, the intelligent reflecting surface (IRS) which can passively perform anomalous reflection, phase shifting, and even polarization control, has emerged as an effective solution to overcome these issues and to assist the wireless systems to satisfy the requirements of the fifth generation (5G) and beyond [1], [2]. The idea of the IRS-enabled programmable wireless environment has quickly attracted much interest. Since then, numerous studies on the IRS's applications in various wireless systems have been published and shown that the IRS can give a remarkable improvement in both performance and security capability.

To evaluate the performance of IRS-aided wireless communications (IRSaWCs), studies on channel characteristic for IRSaWC are essential works. Due to the lack of complete designs for the IRS which allow full operational functions, such as beam steering, phase shifting, etc., the current studies on channel modelling involving the IRSaWCs are mostly based on the theoretical approach.[1] The first approach

The associate editor coordinating the review of this manuscript and approving it for publication was Parul Garg.

[1]The theoretical approach in channel modelling is accepted in the literature, e.g., it is adopted in the works of [3], [4], and [5] for similar studies.

adopted in most studies assumed that the reflecting tiles (RTs) of the IRS can reflect the signals to many positions and the channel via each RT comprises the effects of the reflection coefficient, the transmit-antenna-to-RT and RT-to-receive-antenna channel coefficients which are modeled by widely known fading distributions, such as Rayleigh fading [6], [7], Nakagami-m fading [8] and Rice fading [9], [10], etc.. The second approach considers the reflection on the RT as a perfect anomalous reflection, hence, the incident field is reflected in a specific direction and the reflected links can be considered as alternative LoS (aLoS) links [11], [12], [13]. Although the two approaches exploit some characteristics of the IRS to propose their channel model, they still lack a solid physics analysis of the reflection on the RT, hence, inaccurate assessments can be obtained. To avoid a complex theoretical analysis and data processing, the machine learning method (i.e., generative adversarial network (GAN) [14]) has been adopted to approximate the channel distribution of IRSaWCs. Despite providing good approximation, this approach requires high computation expenses and a large number of channel samples to train the neural network models; therefore, it is not suitable for system design. For these reasons, the authors of [15] proposed using the theory of scattering and physical optics techniques to develop an approximate channel model for IRSaWCs. This channel model can reduce the complexity in calculating the theoretical system performance and allow the system design. Since the work in [15] was investigated in an ideal scenario (e.g., the absence of multi-path fading and the perfect alignment in the incident angles between the IRS and actual field), it is difficult to model the actual wireless channel on which the received signal propagates and the actual wireless channel for IRS-aided multiple-antenna wireless systems (IRSaMAWSs).

In this paper, we analyze and propose a novel channel model for IRSaWC in a practical scenario (i.e., the presences of the multi-path fading, the misalignment in the incident angles and the phase distortion caused by the diffuse scatters). These make our proposed channel model more appropriate to describe the wireless channels for the IRSaWC and IRSaMAWSs. Particularly, the signal at the receive (Rx) antenna is categorized into two groups. We use the theory of the scattered field and the physical optics techniques to analyze the first group that includes the signals reflected from the IRS. Then, we use the modified SV model to analyze the second group that includes the rest of signals. Having analysed the obtained theoretical results, we can construct our proposed channel model. The contributions of our study are summarized as follows:

- We show that even there is a misalignment in the incident angle, the RT can perform the anomalous-reflecting and phase-shifting functions. The actual reflected angle and the squared magnitude function for the scattered field are mathematically computed. Then, the path loss model can be obtained. These important results allow studies on the path loss model for the IRSaMAWS.
- Next, we combine the path loss model and the modified SV model built for the sub-6 Ghz and millimeter wave (mmWave) bands [13] to develop the channel model for the IRSaWC. We show that in the IRSaWC, the information at the destination experiences a Rice fading channel. The theoretical formulas for the K-factor of the Rice fading, the received information signal power, and the received distortion power are derived.
- After that, the obtained results for the channel modelling are extended to the multiple-antenna scenario. The combined signal-to-noise (SNR), which reflects the system performance, is investigated. We propose a gamma distribution-based approximate distribution for the combined SNR and evaluate the outage performance (OP) and achievable rate (AR) of an IRSaMAWS. The accuracy of this approximate distribution is verified via Montes Carlos simulations.
- The results for the OP and AR show that the IRS is an effective solution to enhance the system performance, especially when the LoS link is not available. With a sufficiently large size of the IRS, the signal strength received via the reflected links can be stronger than that received via the LoS link. Although the phase distortion from the IRS causes an additional noise at the receiver, the system performance is enhanced by using more RTs. This benefit is obtained through the signal-combining capability of the IRS. In addition, the effects of important parameters, such as the size of the RT, the phase distortion factor, the number of transmit antennas, and the position of the IRS, on the channel characteristics and the system performance are studied.

The rest of this paper is organized as follows. In Section II, the scattered field and the far-field path loss model over the RT are examined. In Section III, the channel model for IRSaWC is studied. In Section IV, a gamma distribution-based approximate distribution for the combined SNR of an IRSaMAWS is proposed. The conclusions are presented in Section V. Finally, The proofs for the lemmas are presented in the appendix.

Notation: We use $\text{REF}(\theta_1, \theta_2, \varphi)$ to denote the reflection on the RT of a wave field hitting the RT at an angle θ_1 and departing at angle θ_2 with the phase shift φ; we use $\text{A} \rightarrow \text{B}$ to denote the link from a point A to a point B; $\arcsin(\cdot)$ is the inverse sine function; $\angle(r)$ returns the angle of a complex number r in polar form; $\text{sinc}(x) = 1$ if $x = 0$, otherwise $\text{sinc}(x) = \sin(x)/x$; $\delta(c_1, \ldots, c_P) = \delta(c_1) \times \ldots \times \delta(c_P)$ where $\delta(\cdot)$ is the delta function; $x \sim \text{Rayleigh}(\Omega)$ is the Rayleigh distribution with the scale parameter Ω; $x \sim \text{Gamma}(k, \mu)$ is the Gamma distribution with the shape parameter k and the scale parameter μ; $x \sim \text{Rice}(k, \Omega)$ is the Rice distribution with the shape parameter k and the scale parameter Ω; $x \sim \text{Uniform}(a, b)$ is the continuous uniform distribution over interval $(a, b]$; $x \sim \text{CN}(0, N_0)$ is a complex Gaussian distribution with zero mean and variance N_0; $x \sim \text{Truncated-Gaussian}(\cdot; 0, \sigma^2|\theta)$ is the conditional truncated Gaussian distribution for a given

θ with zero mean and variance σ^2; erf$(\cdot)$ is the error function; $u \cdot v$ is the dot product of the two vectors u and v; $\mathbb{E}\cdot$ is the expectation operator; erf$(\cdot)$ is the error function; $\|x\|$ is the ℓ^2 − norm of a complex vector x; $h^\dagger$ is the conjugate transpose of the vector h; $\gamma(\alpha, x)$ is the upper incomplete gamma function [17, Eq. (8.350.1)]; and Γ is the gamma function [17, Eq. (8.350.3)].

II. SCATTERED FIELD CHARACTERIZATION AND FAR-FIELD PATH LOSS MODEL OVER THE IRS

In this section, we characterize the scattered field of an $a \times b$ rectangle RT as illustrated in Fig. 1. We consider a general scenario where there is a slight misalignment in the incident angle between the RT and the actual incident field. Particularly, the RT expects the wave field to arrive at a configured incident angle $\hat{\theta}_{\text{inc}}$ which may differ a bit from the actual incident angle $\theta_{\text{inc}} = \hat{\theta}_{\text{inc}} + \Delta\theta$ where $\Delta\theta$ represents the difference in angle between θ_{inc} and $\hat{\theta}_{\text{inc}}$. The formulas for the electric field (E-field) and the magnetic field (H-field) of a general incident field hitting the RT at an angle θ (use $\theta = \hat{\theta}_{\text{inc}}$ and $\theta = \theta_{\text{inc}}$ to obtain the formulas for the expected and the actual incident fields, respectively) can be written as follows [15].

$$\mathbf{E}_{inc}(\theta) = e_x E_{inc} e^{-j\boldsymbol{\beta}_{inc}(\theta)\cdot r}, \tag{1}$$

$$\mathbf{H}_{inc}(\theta) = e_{inc}(t)\frac{E_{inc}}{\eta} e^{-j\boldsymbol{\beta}_{inc}(\theta)\cdot r}, \tag{2}$$

where E_{inc} is the magnitude of the incident E-field, $\beta = 2\pi/\lambda_0$ is the phase constant, λ_0 is the wavelength, η is the characteristic impedance of the medium, $\boldsymbol{\beta}_{inc}(\theta) = \beta(\sin(\theta)e_y - \cos(\theta)e_z)$ is the phase constant vector which also indicates the propagation direction of the wave plane, r is the position vector in rectangular coordinates, and $e_{inc}(\theta) = -\cos(\theta)\, e_y - \sin(\theta)\, e_z$ is the direction of the H-field.

The RT is configured to reflect the EM field at an angle $\hat{\theta}_{ref}$ with a phase shift φ_0 which is achieved via adjusting the phase profile of the RT $\Phi(x, y)$. Since the behavior of the actual reflected field depends on $\Phi(x, y)$, we study it later. Now, let focus on the expected reflected field on the RT to determine the configured phase profile of the RT. This field must have the form of a wave plane departing at an angle $\hat{\theta}_{ref}$ with a phase shift φ_0. The formulas for E-field and H-field of a general reflected field departing at angle θ (use $\theta = \hat{\theta}_{ref}$ to obtain the formulas for the expected reflected field) are written as

$$\mathbf{E}_{ref}(\theta) = e_x E_{ref} e^{-j\boldsymbol{\beta}_{ref}(\theta)\cdot r + j\varphi_0}, \tag{3}$$

$$\mathbf{H}_{ref}(\theta) = e_{ref}(\theta)\frac{E_{ref}}{\eta} e^{-j\boldsymbol{\beta}_{ref}(\theta)\cdot r + j\varphi_0}, \tag{4}$$

where E_{ref} is the magnitude of the reflected E-field, $\boldsymbol{\beta}(\theta) = \beta(\sin(\theta)e_y + \cos(\theta)e_z)$ is the phase constant vector, and $e_{ref}(\theta) = \cos(\theta)e_y - \sin(\theta)e_z$ is the direction of the reflected H-field.

At the surface of the RT ($z = 0$), the incident field $\left(\mathbf{E}_{inc}(\hat{\theta}_{inc})|_{z=0}, \mathbf{H}_{inc}(\hat{\theta}_{inc})|_{z=0}\right)$ is transformed into the reflected field $\left(\mathbf{E}_{ref}(\hat{\theta}_{ref})|_{z=0}, \mathbf{H}_{ref}(\hat{\theta}_{ref})|_{z=0}\right)$. The phase profile for satisfying the above wave transformation obeys the following rule.

$$\begin{aligned}\Phi(x, y) &= \angle\left(\frac{E_{ref}\, e^{-j\beta \sin\left(\hat{\theta}_{ref}\right)y + j\varphi_0}}{E_{inc} e^{-j\beta \sin\left(\hat{\theta}_{inc}\right)y}}\right), \\ &= \beta\left(\sin\left(\hat{\theta}_{inc}\right)y - \sin\left(\hat{\theta}_{ref}\right)\right)y + \varphi_0. \end{aligned} \tag{5}$$

We assume that the RT only manipulates the reflected field via changing its phase profile. This means that in IRSaWC, when the IRS controller receives a command of reflecting an incident field at an angle $\hat{\theta}_{inc}$ to an angle $\hat{\theta}_{ref}$, it sets the phase profile of the RT using the rule in (5). The phase profile of the RT is the key to determining the actual reflected field on the surface which is presented in Lemma 1.

Lemma 1: Consider a reflection on perpendicular a plane of the RT consisting of the vectors e_z and r. The static phase profile given in (5) for performing a configured anomalous reflection $\text{REF}(\hat{\theta}_{inc}, \hat{\theta}_{ref}, \varphi_0)$ *can also perform an anomalous reflection* $\text{REF}(\theta_{inc}, \theta_{ref}, \varphi_0)$ *where the actual reflected angle θ_{ref} is calculated as*

$$\theta_{ref} = \arcsin\left(\sin\left(\hat{\theta}_{ref}\right) + \sin\left(\theta_{inc}\right) - \sin\left(\hat{\theta}_{inc}\right)\right). \tag{6}$$

Proof: At the surface, the actual reflected E-field corresponding to the actual incident field $\mathbf{E}_{inc}(\theta_{inc})|_{z=0}$ is written as

$$\begin{aligned}\angle\left(\mathbf{E}_{ref}|_{z=0}\right) &= \Phi(x, y) + \angle\left(\mathbf{E}_{inc}(\theta_{inc})\right) \\ &= -\beta \sin(\theta_{ref})y + \varphi_0. \end{aligned} \tag{7}$$

Using (3, 4), it is seen that $\mathbf{E}_{ref}|_{z=0} = \mathbf{E}_{ref}(\theta_{ref})|_{z=0}$. Therefore, the actual reflected H-field on the RT is given by [18, Eq. (4-3)]

$$\mathbf{H}_{ref}(\theta_{ref})\big|_{z=0} = e_{inc}(\theta_{ref})\frac{E_{ref}}{\eta} e^{-j\beta \sin(\theta_{ref})y + j\varphi_0}. \tag{8}$$

In practical scenarios, since the IRS is attached to purposely enhance the signal quality at a specific area, its position setup needs to guarantee $\theta_{ref} \ll 90°$ for performance efficiency. Moreover, the RT's phase profile is set to achieve small values for $\Delta\theta$, equivalently $\hat{\theta}_{inc} \approx \theta_{inc}$. Therefore, the value inside the function $\arcsin(\cdot)$ is in a valid range [-1,1]. It is seen from (7, 8) that the actual reflected field on the RT also has a phase shift φ_0 even there is a misalignment in the incident angle. Lemma 1 is proven. □

Lemma 1 reveals an important property of the reflection on the RT which allows further steps in channel modeling and characterizing. Based on the reflected field on the RT, we investigate the squared magnitude of the scattered field at an arbitrary observation angle $\theta_s \in (-90°, 90°)$.

Lemma 2: The squared magnitude of the scattered field yielded from the reflection of an incident field $(\mathbf{E}_{inc}(\theta_{inc}), \mathbf{H}_{inc}(\theta_{inc}))$ *on a RT, which is purposely configured for a reflection* $\text{REF}(\hat{\theta}_{inc}, \hat{\theta}_{ref}, \varphi_0)$*, is calculated as*

$$S\left(\theta_s; E_{inc}^2, d\right) = \left(\frac{ab}{\lambda_0}\right)^2 \frac{E_{inc}^2}{d^2} \cos\left(\theta_{inc}\right) \cos\left(\theta_{ref}\right)$$

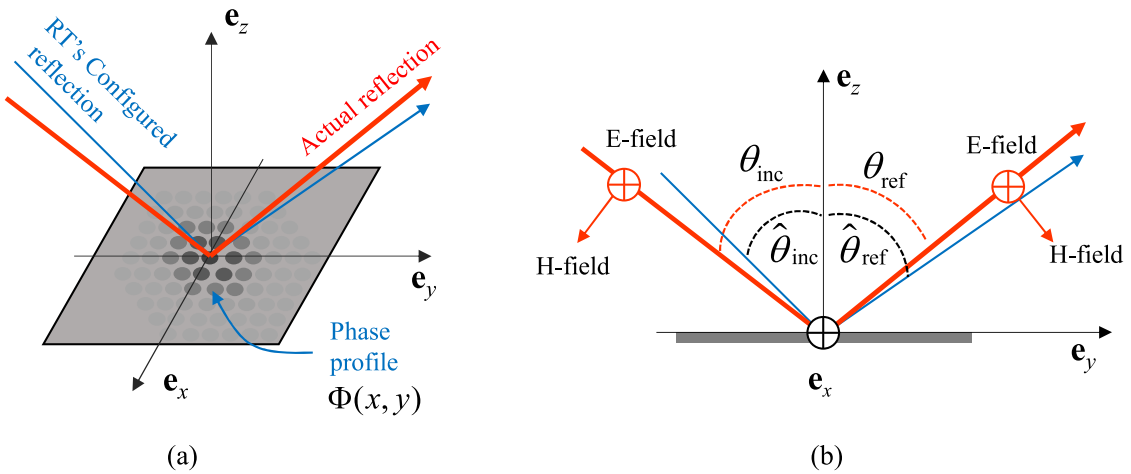

FIGURE 1. (a) The reflection on the RT and (b) the side view of the reflection.

$$\times sinc^2\left(\tfrac{1}{2}b\beta\left(\sin(\theta_s)-\sin\left(\theta_{ref}\right)\right)\right), \quad (9)$$

where d is the distance from the center of the RT to the observer's position.

Proof: The electric current density on the surface ($z = 0$), by neglecting surface edge effects and applying the physic optic technique on the negligible-thickness flat RT [18, Chapter 7.10], can be expressed as $J_S \approx 2e_z \times \mathbf{H}_{ref} = -2e_x \frac{E_{inc}\cos(\theta_{ref})}{\eta} e^{-j\beta\sin(\theta_{ref})y+j\varphi_0}$. Assuming the loss-less reflection on the surface, i.e., $E^2_{inc}\cos(\hat{\theta}_{inc}) = E^2_{ref}\cos(\hat{\theta}_{ref})$, then following the similar steps as in [18, Example 11-3], we can prove Lemma 2. □

To understand the effect of the incident angle on the squared magnitude of the scattered field, the reflections of three fields Field -1, Field -2, Field -3 with their respective incident angles $\theta \in \{55°, 60°, 65°\}$ are investigated. The RT is configured to perform a reflection REF($\hat{\theta}_{inc} = 60°, \hat{\theta}_{ref} = 30°, -$). The results for the normalized squared magnitude $S(\theta_s) = S(\theta_s; E_{inc}, d)\frac{d^2}{E^2_{inc}}$ are plotted in Fig. 2 as the functions of θ_s. Let consider Field -2 (displayed as a middle curve in Fig. 2) which arrives at a correct incident angle $\theta_{inc} = \hat{\theta}_{inc} = 60°$. The reflected field of Field -2 is focused on the configured direction $\theta_{ref} = \hat{\theta}_{ref} = 30°$. At other observation angles $|\theta_s - \theta_{ref}| \gg 0°$, $S(\theta_s)$ receives very small values. The size of the RT significantly influences the shape of $S(\theta_s)$. In particular, a lower normalized squared magnitude and wider beamwidth are observed at the smaller sizes of the RT. For Field -1 and Field -3, the trends for $S(\theta_s)$ follow the similar trend shown for Field -2; however, due to the misalignment in the incident angle, the peaks of the normalized squared magnitudes for Field -1 and Field -3 shift to the reflected angles $\theta_{ref} = \{33.1°, 26.6°\}$, respectively. For the normal size of the RT, such as $a = 10\lambda_0 = 0.5$ meters, these shifts are larger than the 3dB-beamwidth of $S(\theta_s)$. This result point outs an advantage of the IRS in providing highly directional connections, hence reducing the interference in the IRSaWC.

In Fig. 3, we consider a wave field with the incident angle varying in a range $\theta_{inc} \in (45°, 75°)$ and plot the normalized squared magnitude $S(\theta_s)$ at the fixed observation angle $\theta_s = \hat{\theta}_{ref} = 30°$. The RT has the same configuration as in Fig. 2. The normalized squared magnitude reaches its peak when the actual incident angle matches the configured incident angle, i.e., $\theta_{inc} = \hat{\theta}_{inc} = 60°$. For $a = 10\lambda_0$, the 3-dB angle-range is around $\Delta_{3\,\text{dB}} = 3°$, equivalently at a distance 20 meters far from the RT, a maximum position variation is $20 \times \tan(3°) \approx 1.05$ meters. For the multi-antenna base station (BS), this 3-dB angle-range is wide enough to reflect the signals from all antennas to a desired position with good signal strengths. In contrary, the RT with smaller sizes has a larger 3-dB angle-range and gives a lower normalized squared magnitude.

Lemma 3: Using the squared magnitude given in Lemma 2, the path loss model for the signal, that is sent by a transmit (Tx) antenna and reaches a receive (Rx) antenna via a RT, is measured by

$$\alpha_{RT} = \sqrt{\frac{1}{2\eta}\left(\frac{\lambda^2 G_{Rx}(\theta_{Rx\to RT})}{4\pi}\right) S\left(\theta_{RT\to Rx}; E^2_{inc}, d_{RT\to Rx}\right)}, \quad (10)$$

where $E^2_{inc} = \frac{2\eta P_0 G_{Tx}(\theta_{Tx\to RT})}{4\pi d^2_{Tx\to RT}}$ is the squared magnitude of the incident E-field, P_0 is the transmit power, $G_{Tx}(\cdot)$ and $G_{Rx}(\cdot)$ are respectively the directivity models of the Tx and Rx antennas, $\theta_{Tx\to RT}$ is the Tx angle formed by the Tx directivity and the direction from the Tx antenna to the RT, $\theta_{Rx\to RT}$ is the Rx angle formed by the Rx directivity and the direction from the Rx antenna to the RT, and $d_{Tx\to RT}$ and $d_{Rx\to RT}$ are respectively the distances of the Tx → RT and Rx → RT links.

III. CHANNEL MODELING AND CHARACTERIZATION FOR IRSaWC

In this section, we propose a channel model for IRSaWC by using the path loss model in Section II and adopting the modified SV model which effectively characterizes the channel

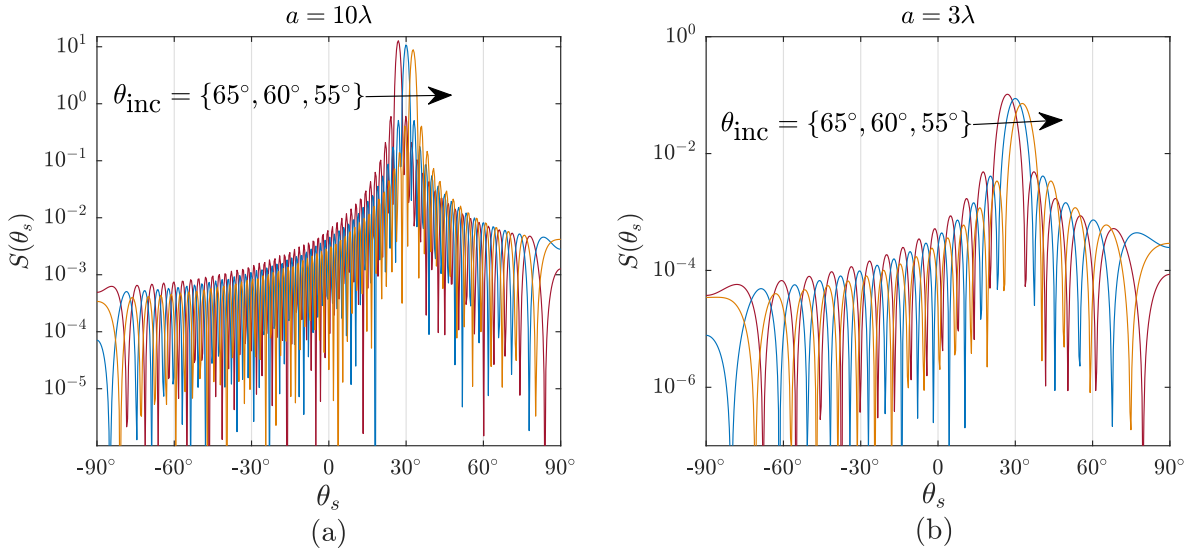

FIGURE 2. The normalized squared magnitude of the scattered field at an arbitrary observation angle $\theta_s \in (-90°, 90°)$. Other setting and parameters: configured reflection rule REF($\hat{\theta}_{inc} = 60°, \hat{\theta}_{ref} = 30°, -$), the actual incident angles for three considered fields $\theta \in \{55°, 60°, 65°\}$.

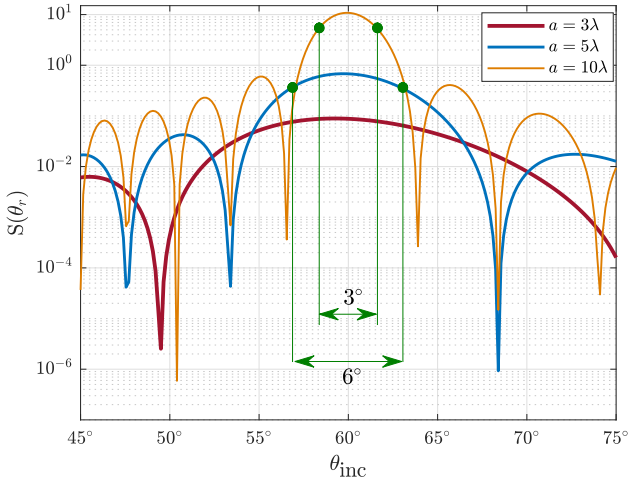

FIGURE 3. The normalized squared magnitude of the scattered field at a fixed observation angle $\theta_s = \hat{\theta}_{ref} = 30°$ with different actual incident angles $\theta_{inc} = \in (45°, 75°)$. Other setting: the RT's configured reflection rule REF($\hat{\theta}_{inc} = 60°, \hat{\theta}_{ref} = 30°, -$).

model for sub-6 GHz and mmWave bands. The signal propagation model is illustrated in Fig. 4 and the channel response for the IRSaWC is written as in (11) as shown at the bottom of the next page, where $\{\alpha_{LoS}, \alpha_{Scatt/LoS}, \alpha_{Scatt/IRS}, \alpha_{Ray(k,l)}, \alpha_{RT(n)}\}$ and $\{|h_{LoS}|, |h_{Scatt/LoS}|, |h_{Scatt/IRS}|, |h_{Ray(k,l)}|, |h_{RT(n)}|\}$ are respectively the path loss models and path loss coefficients of the line-of-sight (LoS) signal, the scattering involving the LoS link, the scattering involving the IRS, the signal traveling on the k-th ray, $k = 1, \ldots, K$, of the l-th cluster, $l = 1, \ldots, L$, and the signal reflected from the n-th RT, $n = 1, \ldots, N$; their respective phase shifts are $\{\kappa_{LoS}, \kappa_{Scatt/LoS}, \kappa_{Scatt/IRS}, \kappa_{Ray(k,l)}, \kappa_{RT(n)}\}$; $\{\theta_{Tx}, \theta_{Rx}, \theta_{RT}^{inc}, \theta_{RT}^{ref}\}$ are the variables for the angles of the Tx directivity, the Rx directivity, the actual incident wave field, and the actual reflected wave field at each RT; $\theta_{Tx\to\{Rx,RT(n)\}}$ is the angle formed by the Tx directivity and the direction from the Tx antenna to the {Rx antenna, n-th RT}; $\theta_{Rx\to\{Tx,RT(n)\}}$ is the angle formed by the Rx directivity and the direction from the Rx antenna to the {Tx antenna, n-th RT}, $\theta_{RT(n)\to\{Tx,Rx\}}$ is the angle formed by the normal vector of the n-th RT the direction from the n-th RT to the {Tx, Rx} antenna; $\theta_{\{Tx,Rx\}:Ray(k,l)}$ is the angle of the k-th ray in the l-th cluster as observed at the {Tx, Rx} antenna using the {Tx, Rx} directivity, respectively; t is the variable for the time; T_l is the time delays of the l-th cluster, and $(T_l + \tau_{(k,l)})$ is the time delays of the k-th ray in l-th cluster; the SV model uses T_l and $\tau_{(k,l)}$ to determine the signal attenuation on the rays and the clusters; $\chi_n \in (0, 1)$ is the distortion factor and $\epsilon \sim \text{CN}(0, 1)$ represents the normalized distortion. The phase distortion is caused by many reasons such as diffuse scatters, the variation of the signal frequencies, etc.; hence, according to the central limit theorem, it is reasonable to model it as a complex Gaussian noise and is unpredictable at the receiver. We use $T = \{T_l\}_{l=1}^{L}$, $\boldsymbol{\tau} = \{\tau\}_{(k,l)=(1,1)}^{(K,L)}$, $\boldsymbol{\theta} = \left\{\theta_{X\to Y}|_{X,Y\in Tx,Rx,RT(n)}, \theta_{\{Tx,Rx\}:Ray(k,l)}|_{(k,l)=(1,1)}^{(K,L)}\right\}$ to respectively denote the groups of parameters involving the time delays of the clusters, the time delays of the rays in the clusters, and the angles.

Next, we study the path loss models and the path loss coefficients in (11). The path loss model includes the effects of (i) the directivity models $G_{Tx}(\theta_{Tx})$ and $G_{Rx}(\theta_{Rx})$, (ii) the angle of departure (AoD) and angle of arrival (AoA) of the rays, clusters, LoS link and aLoS links (here, we use "aLoS links" for the reflection links to emphasize the capability of providing stable oriented communication links of the IRS), (iii) the time delay models for the rays and clusters.

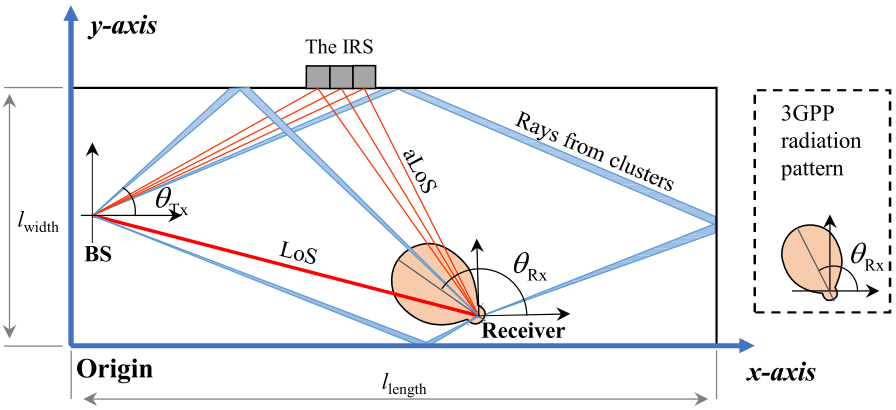

FIGURE 4. The illustration for the signal propagation in the IRSaWC. The signals travel on the LoS link, the aLoS links and the rays before reaching the Rx antenna.

In this study, we consider two ordinary directivity models for the transceiver antenna, one is equal-gain model where $G_{Tx}(\theta_{Tx}) = G_{Rx}(\theta_{Rx}) = 1, \forall(\theta_{Tx}, \theta_{Rx})$, and another introduced in 3GPP standard as [19]

$$G(\theta) = \begin{cases} 10^{-0.3(\theta/\theta_{3\,\text{dB}})^2} & ;\text{if } |\theta| < \theta_c, \\ 0.01 & ;\text{otherwise}, \end{cases} \tag{12}$$

where $\theta_{3\,\text{dB}}$ is the 3-dB antenna beamwidth, $\theta_c = \theta_{3\,\text{dB}}\sqrt{20/3}$ is the positive intersection point of the two sub-functions in (12). Since it is possible to determine the AoD and AoA for the clusters, LoS link and aLoS links, using ray tracing techniques, in the follows we investigate the AoD/AoA for the rays. The truncated Gaussian distribution is adopted to describe the distribution of the AoD/AoA of the rays in each cluster. Let θ_l^{Tx} and θ_l^{Rx} be respectively the AoD and AoA of the l-th cluster, $l = 1, \ldots, L$, the distribution of the AoD and AoA of each ray in l-th cluster obeys the distribution Truncated-Gaussian$(x; 0, \sigma^2|\theta_l)$ given as follows.

$$p(x|\theta_l) = \frac{C_0}{\sqrt{2\pi}\sigma}\exp\left(-\frac{(x-\theta_l)}{2\sigma^2}\right) w(x, \theta_l - \Delta, \theta_l + \Delta), \tag{13}$$

where Δ defines the range of the truncated Gaussian distribution, $C_0 = 1/(\Phi(\Delta/\sigma) - \Phi(-\Delta/\sigma))$ is a constant guaranteeing $\int_{\theta_l-\Delta}^{\theta_l-\Delta} p(x|\theta_l)dx = 1$, $\Phi(x) = \frac{1}{2}\left[1 + \text{erf}(\frac{x}{\sqrt{2}})\right]$, $\theta_l := \theta_l^{\{Tx,Rx\}}$ is the AoD/AoA of the l-th cluster and $w(x, a, b)$ is a rectangular window function given as

$$w(x, a, b) = \begin{cases} 1 & ;\text{if } x \in [a, b], \\ 0 & ;\text{otherwise}, \end{cases} \tag{14}$$

According to [20], the time delay models for the clusters and the rays respectively obey the following rules

$$p(T_{l+1}|T_l) = \Lambda e^{-\Lambda(T_{l+1}-T_l)}, \text{where } l = 1, \ldots, L, \tag{15}$$

$$p(\tau_{k+1,l}|\tau_{k,l}) = \lambda e^{-\lambda(\tau_{k+1,l}-\tau_{k,l})}, \text{where } k = 2, \ldots, K, \tag{16}$$

where $T_0 = \tau_{1,l} = 0$, Λ and λ are respectively the cluster and ray arrival rates.

Using the above assumptions, the path loss coefficients in (11) can be derived as in Table 1 where Γ and γ are respectively the cluster and ray power delay time constants, $\zeta_{Scatt/LoS} \in (0, 1)$ and $\zeta_{Scatt/IRS} \in (0, 1)$ are the scattering signal power factors involving the LoS and the IRS, respectively. In addition, we can separate (11) into three groups that respectively include the effects of (i) the LoS link and aLoS

$$\begin{aligned} &h\left(t, \theta_{Tx}, \theta_{Rx}, \theta_{RT}^{inc}, \theta_{RT}^{ref}|T, \boldsymbol{\tau}, \boldsymbol{\theta}\right) \\ &= \underbrace{\alpha_{LoS}\delta\left(\theta_{Tx} - \theta_{Tx\to Rx}; \theta_{Rx} - \theta_{Rx\to Tx}\right)}_{|h_{LoS}|} e^{j\kappa_{LoS}} + \underbrace{\alpha_{Scatt/LoS}}_{|h_{Scatt/LoS}|} e^{j\kappa_{Scatt/LoS}} + \underbrace{\alpha_{Scatt/IRS}}_{|h_{Scatt/IRS}|} e^{j\kappa_{Scatt/IRS}} \\ &\quad + \sum_{l=1}^{L}\sum_{k=1}^{K} \underbrace{\alpha_{Ray(k,l)}\delta\left(t - T_l - \tau_{(k,l)}; \theta_{Tx} - \theta_{Tx:Ray(k,l)}; \theta_{Rx} - \theta_{Rx:Ray(k,l)}\right)}_{|h_{Ray(k,l)}|} e^{j\kappa_{Ray(k,l)}} \\ &\quad + \sum_{n=1}^{N} \underbrace{\alpha_{RT(n)}\delta(\theta_{Tx} - \theta_{Tx\to RT(n)}; \theta_{RT}^{inc} - \theta_{RT(n)\to Tx}; \theta_{RT}^{ref} - \theta_{RT(n)\to Rx}; \theta_{Tx} - \theta_{Rx\to RT(n)})}_{|h_{RT(n)}|} \\ &\quad \times \left(\sqrt{1-\chi_n} + \sqrt{\chi_n}\epsilon_n\right) e^{j\kappa_{RT(n)} + j\varphi_{RT(n)}}, \end{aligned} \tag{11}$$

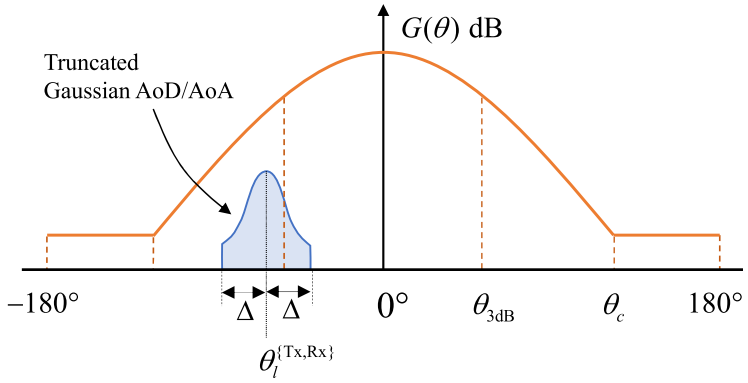

FIGURE 5. The illustration for AoD and AoA at a receive antenna.

links, (ii) the rays and scattering, and (iii) the phase distortion as the follows.

$$h(t) := h\left(t, \theta_{Tx}, \theta_{Rx}, \theta_{RT}^{inc}, \theta_{RT}^{ref} | T, \boldsymbol{\tau}, \boldsymbol{\theta}\right) = h_{Signal} + h_{PD} \tag{17}$$

where

$$h_{Signal} = h_{LoS+aLoS} + h_{Ray/Cluster+Scatt}, \tag{18}$$

$$h_{LoS+aLoS} = |h_{LoS}| e^{j\kappa_{LoS}} + \sum_{n=1}^{N} \sqrt{1-\chi_n} |h_{RT(n)}| e^{j\kappa_{RT(n)} + j\varphi_{RT(n)}}, \tag{19}$$

$$h_{Ray/Cluster+Scatt} = \left|h_{Scatt/LoS}\right| e^{j\kappa_{Scatt/LoS}} + \left|\alpha_{Scatt/IRS}\right| e^{j\kappa_{Scatt/IRS}} + \sum_{l=1}^{L} \sum_{k=1}^{K} \left|h_{Ray(k,l)}\right| e^{j\kappa_{Ray(k,l)}}, \tag{20}$$

$$h_{PD} = \sum_{n=1}^{N} \left|h_{RT(n)}\right| \sqrt{\chi_n} \epsilon_n e^{j\kappa_{RT(n)} + j\varphi_{RT(n)}}. \tag{21}$$

When an information signal propagates over $h(t)$, the following results can be obtained. Firstly, since h_{PD} cannot carry any information, it causes an additional noise at the receiver with the distortion power defined as

$$\Omega_{PD} = \mathbb{E}\{|h_{PD}|^2\}. \tag{22}$$

Secondly, from (18, 19, 20), it is seen that the information signal received at the receiver is experienced a channel h_{Signal} that obeys a Rice distribution with the scale parameter Ω_{Signal} and shape parameter K respectively given by

$$\Omega_{Signal} = \mathbb{E}\{|h_{LoS+aLoS}|^2\} + \mathbb{E}\{|h_{Ray/Cluster+Scatt}|^2\}, \tag{23}$$

$$K = \frac{\mathbb{E}\{|h_{LoS+aLoS}|^2\}}{\mathbb{E}\{|h_{Ray/Cluster+Scatt}|^2\}}. \tag{24}$$

Lemma 4: With a given setup for the RT's phase shifts, $\varphi_n, n = 1, \ldots, N$. The expressions for $\mathbb{E}\{|h_{LoS+aLoS}|^2\}$ and $\mathbb{E}\{|h_{PD}|^2\}$ are respectively given as

$$\mathbb{E}\{|h_{LoS+aLoS}|^2\} = \left(|h_{LoS}| + \sum_{n=1}^{N} \sqrt{1-\chi_n} \left|h_{RT(n)}\right| \times \cos\left(\kappa_{RT(n)} + \varphi_{RT(n)} - \kappa_{LoS}\right)\right)^2 + \left(\sum_{n=1}^{N} \sqrt{1-\chi_n} \times \left|h_{RT(n)}\right| \sin\left(\kappa_{RT(n)} + \varphi_{RT(n)} - \kappa_{LoS}\right)\right)^2. \tag{25}$$

$$\mathbb{E}\{|h_{PD}|^2\} = \left(\sum_{n=1}^{N} \sqrt{\chi_n} \left|h_{RT(n)}\right| \cos\left(\kappa_{RT(n)} + \varphi_{RT(n)}\right)\right)^2 + \left(\sum_{n=1}^{N} \sqrt{\chi_n} \left|h_{RT(n)}\right| \sin\left(\kappa_{RT(n)} + \varphi_{RT(n)}\right)\right)^2. \tag{26}$$

Proof: We consider (19) as the sum of constant vectors. Let set the LoS link as a reference vector, (25) can be proven using the vector projection of each aLoS link onto the reference vector and using vector rejection of each aLoS link from the reference vector. Using similar approaches, (26) can be also proven. □

Additionally, using the vector addition method, it is easy to show that $\mathbb{E}\{|h_{LoS+aLoS}|^2\}$ is maximized when the IRS's phase shifts obey the following rule.

$$\varphi_{RT(n)} = \kappa_{LoS} - \kappa_{RT(n)}. \tag{27}$$

Lemma 5: The expression for $\mathbb{E}\{|h_{Ray/Cluster+Scatt}|^2\}$ is given in (28), as shown at the bottom of the next page, where $\mathbb{A} = \frac{(\Lambda\Gamma)^l}{(1+\Lambda\Gamma)^l}$ and $\mathbb{B} = \frac{(\lambda\gamma)^{k-1}}{(1+\lambda\gamma)^{k-1}}$. For the case of equal-gain model, $\mathbb{C}$ and $\mathbb{D}$ are determined as $\mathbb{C}_{EqG} = \mathbb{D}_{EqG} = 1$. For the case of 3GPP-standard directivity model, $\mathbb{C}$ and $\mathbb{D}$ are determined in Table 2 where $\hat{\sigma}_0 = \sigma \left(\frac{0.6\ln(10)\sigma^2}{\theta_{3\text{dB}}^2} + 1\right)^{-1/2}$.

Proof: Using the distribution characteristics of $|h_{Scatt/LoS}|^2$ and $|h_{Scatt/IRS}|^2$ in Table 1, we can compute $\mathbb{E}\{|h_{Scatt/LoS}|^2\}$ and $\mathbb{E}\{|h_{Scatt/IRS}|^2\}$. For the equal-gain model, the directivity functions is $G_{\{Tx,Rx\}}(\theta) = 1, \forall\theta$ hence,

TABLE 1. Path loss coefficients, phase shifts and distributions of elements in (11).

$\theta_{\mathrm{Tx}\to Rx}, \theta_{\mathrm{Rx}\to Tx}, \theta_{\{Tx,Rx\}\to RT(n)}, \theta_{\{Tx,Rx\}\to IRScenter}$	$\sim$ The values of these variables depend on the device's position configuration.
$\theta_{\mathrm{Tx}:Ray(k,l)}, \theta_{\mathrm{Rx}:Ray(k,l)}$	$\sim$ Truncated-Gaussian$(\cdot\|\theta_l^{\{Tx,Rx\}})$ and their values are randomly generated. on each time slot of the communication $\phi_l^{\{Tx,Rx\}}$ is the cluster AoD or AoA (See Fig. 5 and Table 3 for more information.)
$\|h_{\mathrm{LoS}}\|^2$	$=\sqrt{\frac{\lambda_0^2 G_{\mathrm{Tx}}(\theta_{\mathrm{Tx}\to Rx}) G_{\mathrm{Rx}}(\theta_{\mathrm{Rx}\to Tx}) P_0}{(4\pi d_{\mathrm{Tx}\to Rx})^2}}$
$\|h_{\mathrm{Scatt}/LoS}\|$	$\sim$ Rayleigh $\left(\sqrt{\frac{\lambda_0^2 G_{\mathrm{Tx}}(\theta_{\mathrm{Tx}\to Rx}) G_{\mathrm{Rx}}(\theta_{\mathrm{Rx}\to Tx}) \bar{\beta}_0 \zeta_{\mathrm{Scatt}/LoS}}{(4\pi d_{\mathrm{Tx}\to Rx})^2}}\right)$
$\|h_{\mathrm{Scatt}/IRS}\|$	$\sim$ Rayleigh $\left(\sqrt{\frac{\lambda_0^2 G_{\mathrm{Tx}}(\theta_{\mathrm{Tx}\to IRScenter}) G_{\mathrm{Rx}}(\theta_{\mathrm{Rx}\to IRScenter}) \bar{\beta}_0 \zeta_{\mathrm{Scatt}/IRS}}{(4\pi (d_{\mathrm{Tx}\to IRScenter}+d_{\mathrm{Rx}\to IRScenter}))^2}}\right)$
$\|h_{\mathrm{Ray}(k,l)}\|$	$\sim$ Rayleigh $\left(\sqrt{\frac{\lambda_0^2 G_{\mathrm{Tx}}(\theta_{\mathrm{Tx}:Ray(k,l)}) G_{\mathrm{Rx}}(\theta_{\mathrm{Rx}:Ray(k,l)}) \bar{\beta}_0}{(4\pi d_{\mathrm{Tx}\to Rx})^2} \exp\left(-\frac{T_l}{\Gamma}-\frac{\tau_{(k,l)}}{\gamma}\right)}\right)$
$\|h_{\mathrm{RT}(n)}\|$	$=\sqrt{\frac{\lambda_0^2 G_{\mathrm{Rx}}(\theta_{\mathrm{Rx}\to RT(n)})}{8\eta\pi} S\left(\theta_{\mathrm{RT}(n)\to \mathrm{Rx}}; \frac{2\eta P_0 G_{\mathrm{Tx}}(\theta_{\mathrm{Tx}\to RT(n)})}{4\pi d_{\mathrm{Tx}\to RT(n)}^2}, d_{\mathrm{RT}(n)\to \mathrm{Rx}}\right)}$
$\kappa_{LoS}, \kappa_{\mathrm{RT}(n)}$	$\sim$ Uniform$(-180°, 180°)$ and are constants during communication.
$\kappa_{\mathrm{Ray}(k,l)}, \kappa_{\mathrm{Scatt}/loS}$ $\kappa_{\mathrm{Scatt}/IRS}$	$\sim$ Uniform$(-180°, 180°)$ and their values are randomly generated on each time slot of the communication.

we can have $\mathbb{C}_{EqG} = \mathbb{D}_{EqG} = 1$. Using (15,16), results for $\mathbb{A}$ and $\mathbb{B}$ can be easily proven [16]. Finally, the results for $\mathbb{C}_{3GPP}$ and $\mathbb{D}_{3GPP}$ are proven in Appendix V. □

To study the trends of the K factor, the received information signal power, and the received distortion power, we plot them as the functions of the Rx directivity, $\theta_{Rx} \in (-180°, 180°]$, as shown in Fig. 6. We use the setup as illustrated in Fig. 4, details of the simulation parameters are presented in Table 3 and the IRS's phase shifts are configured as same as those in (27). To verify the effectiveness of the IRS in enhancing the channel quality, three important scenarios of IRSaWC are investigated, (i) in one, the LoS link is available, and the IRS is not used (with-LoS-non-IRS), (ii) in the another, both the LoS link and the IRS are absent (non-LoS-non-IRS), and (iii) in the last one, the LoS link is unavailable and the IRS is employed to assist the communication (non-LoS-with-IRS). As shown that, the Rx information signal strengths and the K factors archive high values in the with-LoS-non-IRS and the non-LoS-with-IRS scenarios and they receive low values in the non-LoS-non-IRS scenario. These results indicate that the IRS efficiently enhances the channel quality in the absence of the LoS link. The effect of the number of the RT on improving the system performance is studied in Figs. 7 and 8. The Rx directivity gives a remarkable influence on the channel quality and the optimal Rx directivity is as follows. In the presence of the LoS/aLoS links, the Rx antenna should be respectively rotated toward the BS/IRS, otherwise, it should be rotated toward Cluster 1 (L1) to yield the best channel quality. The results for different Tx antennas of the multiple-antenna BS show similar trends. This can be explained using the 3-dB angle-range (discussed in Fig.3). In the non-LoS-with-IRS scenario, the received distortion power and the received information signal power reach their largest values at a same Rx directivity; hence, the phase distortion can reduce the advantages of the IRS. This influence is studied in Figs. 7 and 8.

IV. GAMMA DISTRIBUTION-BASED COMBINED- SNR DISTRIBUTION APPROXIMATION AND APPLICATIONS

In Section III, the channel coefficient between a Tx antenna and a Rx antenna in the presence of an IRS was studied. In addition, the results in Figs. 4 and 6 showed that

$$\begin{aligned}\mathbb{E}\{|h_{Ray/Cluster+Scatt}|^2\} &= \mathbb{E}\{|h_{Scatt/LoS}|^2\} + \mathbb{E}\{|h_{Scatt/IRS}|^2\} + \sum_{l=1}^{L}\sum_{k=1}^{K}\mathbb{E}\{|h_{Ray(k,l)}|^2\} \\ &= \frac{\lambda_0^2 G_{Tx}(\theta_{Tx\to Rx}) G_{Rx}(\theta_{Rx\to Tx}) \bar{\beta}_0 \zeta}{(4\pi d_{Tx\to Rx})^2} + \frac{\lambda_0^2 G_{Tx}(\theta_{Tx\to IRScenter}) G_{Rx}(\theta_{Rx\to IRScenter}) \bar{\beta}_0 (1-\zeta)}{(4\pi (d_{Tx\to IRScenter} + d_{Rx\to IRScenter}))^2} \\ &+ \frac{\lambda_0^2 \bar{\beta}_0}{(4\pi d_{Tx\to Rx})^2} \sum_{l=1}^{L}\sum_{k=1}^{K} \underbrace{\mathbb{E}_{T_l}\left\{\exp\left(-\frac{T_l}{\Gamma}\right)\right\}}_{\mathbb{A}} \underbrace{\mathbb{E}_{\tau_{(k,l)}}\left\{\exp\left(-\frac{\tau_{(k,l)}}{\gamma}\right)\right\}}_{\mathbb{B}} \\ &\times \underbrace{\mathbb{E}_{\theta_{Tx:Ray(k,l)}}\{G_{Tx}(\theta_{Tx:Ray(k,l)})\}}_{\mathbb{C}} \underbrace{\mathbb{E}_{\theta_{Rx:Ray(k,l)}}\{G_{Rx}(\theta_{Rx:Ray(k,l)})\}}_{\mathbb{D}},\end{aligned} \tag{28}$$

TABLE 2. Calculations for four cases of $\mathbb{C}_{3GPP}$ and $\mathbb{C}_{3GPP}$.

Cases	Range of θ_l	$\{\mathbb{C},\mathbb{D}\}_{3\text{GPP}}$
1	$\theta_l \in [-\theta_c+\Delta, \theta_c-\Delta]$	$= \frac{C_0 \exp\left(-\frac{0.3\ln(10)\theta_l^2}{0.6\ln(10)\sigma^2+\theta_{3\text{dB}}^2}\right)}{\sqrt{\frac{0.6\ln(10)\sigma^2}{\theta_{3\text{dB}}^2}+1}} \left(\begin{array}{l}\Phi\left(\frac{\theta_l}{\tilde{\sigma}}\left(\frac{0.6\ln(10)\sigma^2}{0.6\ln(10)\sigma^2+\theta_{3\text{dB}}^2}\right)+\frac{\Delta}{\tilde{\sigma}}\right)\\ -\Phi\left(\frac{\theta_l}{\tilde{\sigma}}\left(\frac{0.6\ln(10)\sigma^2}{0.6\ln(10)\sigma^2+\theta_{3\text{dB}}^2}\right)-\frac{\Delta}{\tilde{\sigma}}\right)\end{array}\right)$
2	$\theta_l \in [-\theta_c-\Delta, -\theta_c+\Delta)$	$= 0.01C_0\left(\Phi\left(-\frac{\theta_c+\theta_l}{\sigma}\right)-\Phi\left(-\frac{\Delta}{\sigma}\right)\right)$ $+\frac{C_0 \exp\left(-\frac{0.3\ln(10)\theta_l^2}{0.6\ln(10)\sigma^2+\theta_{3\text{dB}}^2}\right)}{\sqrt{\frac{0.6\ln(10)\sigma^2}{\theta_{3\text{dB}}^2}+1}} \left(\begin{array}{l}\Phi\left(\frac{\theta_l}{\tilde{\sigma}}\left(\frac{0.6\ln(10)\sigma^2}{0.6\ln(10)\sigma^2+\theta_{3\text{dB}}^2}\right)+\frac{\Delta}{\tilde{\sigma}}\right)\\ -\Phi\left(-\frac{\theta_c}{\tilde{\sigma}}-\frac{\theta_l}{\tilde{\sigma}}\frac{\theta_{3\text{dB}}^2}{0.6\ln(10)\sigma^2+\theta_{3\text{dB}}^2}\right)\end{array}\right)$
3	$\theta_l \in (\theta_c-\Delta, \theta_c+\Delta]$	$= \frac{C_0 \exp\left(-\frac{0.3\ln(10)\theta_l^2}{0.6\ln(10)\sigma^2+\theta_{3\text{dB}}^2}\right)}{\sqrt{\frac{0.6\ln(10)\sigma^2}{\theta_{3\text{dB}}^2}+1}} \left(\begin{array}{l}\Phi\left(\frac{\theta_c}{\tilde{\sigma}}-\frac{\theta_l}{\tilde{\sigma}}\frac{\theta_{3\text{dB}}^2}{0.6\ln(10)\sigma^2+\phi_{3\text{dB}}^2}\right)\\ -\Phi\left(\frac{\theta_l}{\tilde{\sigma}}\left(\frac{0.6\ln(10)\sigma^2}{0.6\ln(10)\sigma^2+\theta_{3\text{dB}}^2}\right)-\frac{\Delta}{\tilde{\sigma}}\right)\end{array}\right)$ $+0.01C_0\left(\Phi\left(\frac{\Delta}{\sigma}\right)-\Phi\left(\frac{\phi_c-\phi_l}{\sigma}\right)\right)$
4	Otherwise	$= 0.01$

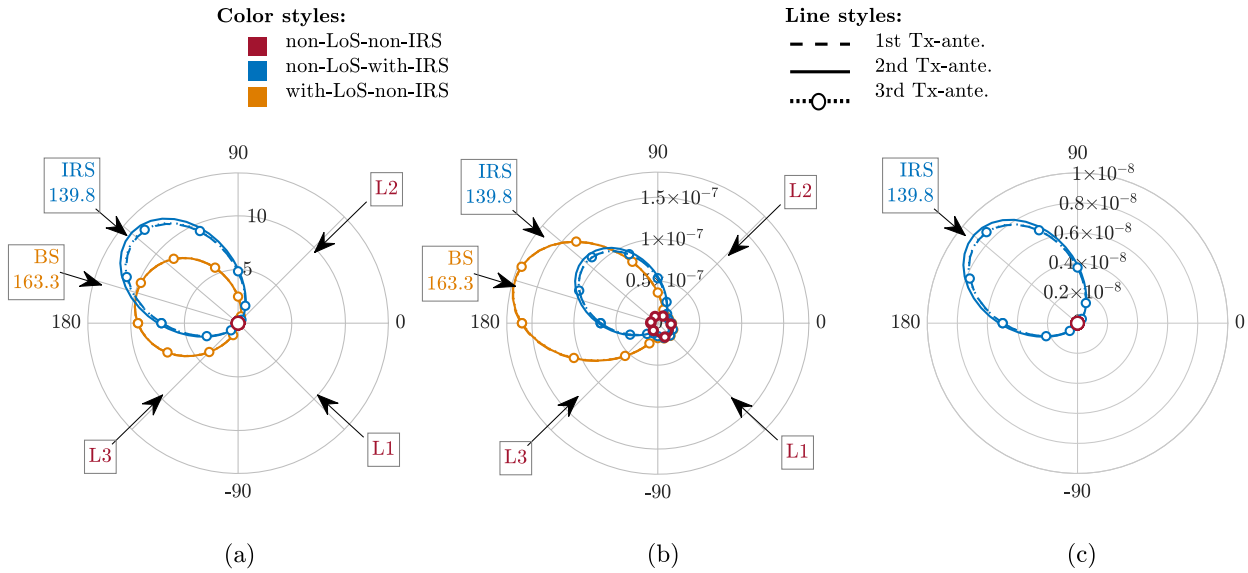

FIGURE 6. The results for (a) the K-factor, (b) the received information signal power and (c) the received distortion power with respect to different Rx antenna's direction.

the IRS is able to reflect all signals from the antennas of a multiple-antenna BS to each Rx antenna due to the short distance between these antennas. This leads to the need for studies on the combined SNR for IRSaMAWS. Since the Rice distribution causes difficulty to the theoretical approach, in this section, we develop a gamma distribution-based combined SNR approximate distribution that facilitates the theoretical analysis for system performance of IRSaMAWS. We consider an IRS-aided maximum-ratio-transmission (MRT) wireless system (IRSaMRTWS) where a M-antenna BS adopts the MRT technique to achieve the combined SNR at a single-antenna receiver with the help of a N-RT IRS (The results for the IRS-aided maximal-ratio-combining can be derived using similar approach).

Let $h(t) = h_{Signal}(t) + h_{PD}(t)$ where $h_{Signal}(t) \sim \text{Rice}(\mathbf{K}, \mathbf{\Omega}_{Signal})$ and $h_{PD}(t) \sim \text{CN}(0, \mathbf{\Omega})$ denote the channel vector between the source and the receiver. We assume the channel is a slow fading and the channel estimation interval is large enough to estimate h_{Signal}. The weight vector for MRT is given as $w(t) = \frac{h_{Signal}^{\dagger}(t)}{\|h_{Signal}(t)\|}$ [21]. The parameters $\mathbf{K} = [K^{(1)}, \ldots, K^{(M)}]$, $\mathbf{\Omega}_{Signal} = [\Omega_{Signal}^{(1)}, \ldots, \Omega_{Signal}^{(M)}]$ and $\mathbf{\Omega}_{PD} = [\Omega_{PD}^{(1)}, \ldots, \Omega_{PD}^{(M)}]$ are obtained using (22, 23, 24). When the BS broadcasts an information signal $x(t)$, the received signal at the receiver is expressed as

$$\begin{aligned} y(t) &= \left(h_{Signal}(t) + h_{PD}(t)\right) w(t)x(t) + n(t) \\ &= \underbrace{\|h_{Signal}(t)\|x(t)}_{Information} + \underbrace{h_{PD}(t)w(t)x(t) + n(t)}_{Overall\ noise} \end{aligned} \quad (29)$$

The combined SNR at the receiver is given by

$$\gamma_{SNR} = \frac{\|h_{Signal}(t)\|^2}{|h_{PD}(t)w(t)|^2 + N_0} \approx \frac{\|h_{Signal}(t)\|^2}{\bar{\Omega}_{PD} + N_0} \quad (30)$$

TABLE 3. The parameters for simulation in Figs. 6, 7 and 8.

The room's size	$l_{length} = 40, l_{width} = 20$ (meters).
The IRS setup	Each RT is configured signals from the midle Tx antenna to the Rx antenna with optimized phase shift $\varphi^*_{\mathrm{RT}(n)}$ which make the reflected information signal has a same phase with the LoS information signal. The RT's size: $a \times b = 0.5 \times 0.5$ (meter^2). The RT's center coordinate: $\mathrm{RT}_x(n) = (n - 0.5(N+1))a + 7.5$ (meters), $\mathrm{RT}_y(n) = 20$ (meters).
Powers (dBm)	$P_0 = 10(\mathrm{d}Bm), \beta_0 = 0(\mathrm{d}Bm), N_0 = -80(\mathrm{d}Bm)$
Tx radiation patterns	Equal gain model.
Rx radiation patterns	3GPP standard.
Tx antenna coordinates (meters)	1st ante. (0, 15.1), 2nd ante. (0, 15), and 3rd ante. (0, 14.9).
Rx antenna coordinate	(30, 1) (meters)
Number of rays & clusters	$L = 3, K = 10$.
Parameters for rays & clusters	$\{\Gamma = 60\mathrm{e}-9, \gamma = 20\mathrm{e}-9, \Lambda = 1/(300\mathrm{e}-9), \lambda = 1/(5\mathrm{e}-9)\}$ [16]. Cluster AoD: $\{\theta_1^{\mathrm{Tx}}, \theta_2^{\mathrm{Tx}}, \theta_3^{\mathrm{Tx}}\} = \{30^\circ, -30^\circ, 60^\circ\}$ for each Tx antenna. Cluster AoA: $\{\theta_1^{\mathrm{Rx}}, \theta_2^{\mathrm{Rx}}, \theta_3^{\mathrm{Rx}}\} = \{-45^\circ, 45^\circ, -135^\circ\}$ for the Rx antenna.
Parameters of the truncated Gaussian distribution	$\Delta = 22.5^\circ, \delta = 45^\circ$,
Parameters for 3GPP radiation pattern	$\theta_{3\mathrm{dB}} = 45^\circ, \theta_c = \sqrt{\frac{20}{3}}\theta_{3\mathrm{dB}} \approx 116.2^\circ$,
Other parameters	$f_0 = 6(\mathrm{GHz}), \lambda_0 = 0.05(\mathrm{meters})$, $\zeta_{\mathrm{Scatt}/LoS} = \zeta_{\mathrm{Scatt}/IRS} = 0.5, \chi_n = 0.2$,

where $n(t) \sim \mathrm{CN}(0, N_0)$ is the additive Gaussian white noise (AGWN) at the receive antenna and the approximation in (30) is based on the fact that the distortion powers caused by difference Tx antennas of the BS receive similar values $\Omega_{PD}^{(m)} \approx \bar{\Omega}_{PD} = \frac{1}{M}\sum_{m=1}^{M}\Omega_{PD}^{(m)}$.

Since γ_{SNR} involves the sum of squared magnitude of Rice random variables (RVs), deriving its exact distribution function is a complex work; moreover, the infinite summations inside this exact result require a high computational cost and is difficult to extend for further calculations. For these reasons, we propose to use a simplifier distribution shown in Lemma 6 to approximate the distribution function of γ_{SNR}.

Lemma 6: Let consider a random vector $X = [X_1, \ldots, X_M]$ *in which* $X_m \sim \mathrm{Rice}(k_m, \Omega_m)$ *The distribution of* $\|X\|^2$ *can be approximated by a gamma distribution as* $\|X\|^2 \approx \|\breve{X}\|^2 \sim \mathrm{Gamma}(k_\Sigma, \mu_\Sigma)$ *with shape and scale parameters given by*

$$k_\Sigma = \frac{\left(\sum_{m=1}^{M}\Omega_m\right)^2}{\sum_{m=1}^{M}\Omega_m^2/\breve{k}_m}, \tag{31}$$

$$\mu_\Sigma = \sum_{m=1}^{M}\Omega_m, \tag{32}$$

where $\breve{k}_m = 1 + k_m^2/(2k_m+1)$.

Proof: Since the distribution of $|X_m|^2$ can be tightly approximated by $|X_m|^2 \approx |\breve{X}_m|^2 \sim \mathrm{Gamma}(\breve{k}_m, \breve{\mu}_m)$ with shape parameter $\breve{k}_m = 1 + k_m^2/(2k_m+1)$ [22] and the scale parameter $\breve{\mu}_m = \Omega_m/\breve{k}_m$, we have an approximation as $\|\boldsymbol{X}\|^2 \approx \|\breve{X}^2\|$ with $\breve{X} = [\breve{X}_1, \ldots, \breve{X}_M]$. $\|\breve{X}^2\|$ is a linear combination of independent non-identical gamma distributed RVs. Using the Welch–Satterthwaite equation, we can approximate $\|\breve{X}^2\|$ by a gamma distribution with the effective degrees of freedom given in (31) and its respective scale parameter given in (32). Lemma 6 is proven. □

Using Lemma 6, we measure two important performance metrics, the outage probability (OP) and the achievable rate (AR) for our considered IRSaMRTWS. We can show that $\gamma_{SNR} \approx \breve{\gamma}_{SNR} \sim \mathrm{Gamma}(k_{SNR}, \mu_{SNR})$ with its parameters given by

$$k_{SNR} = \frac{\left(\sum_{m=1}^{M}\Omega_{Signal}^{(m)}\right)^2}{\sum_{m=1}^{M}(\Omega_{Signal}^{(m)})^2/K^{(m)}}, \tag{33}$$

$$\mu_{SNR} = \frac{\sum_{m=1}^{M}\Omega_{Signal}^{(m)}}{\bar{\Omega}_{PD} + N_0}, \tag{34}$$

The OP and AR of the considered system are calculated as [23]

$$OP = \Pr\left(\gamma_{SNR} < x\right) \approx \frac{1}{\Gamma(k_{SNR})}\gamma\left(k_{SNR}, \frac{x}{\theta_{SNR}}\right), \tag{35}$$

$$AR = \mathbb{E}\left\{\log_2\left(1+\gamma_{SNR}\right)\right\} = \frac{1}{\Gamma(k_{SNR})\theta_{SNR}^{k_{SNR}}} \times \int_0^\infty \log_2\left(1+x\right)x^{k_{SNR}-1}e^{-x/\mu_{SNR}}dx. \tag{36}$$

For integer values or approximate integer values for k_{SNR}, the closed-form expression for AR can be easily obtained using the similar approach in [24, Proposition 3] and some manipulations.

Figs. 7 and 8 respectively plot the optimal OP and optimal AR of our considered system as the functions of various

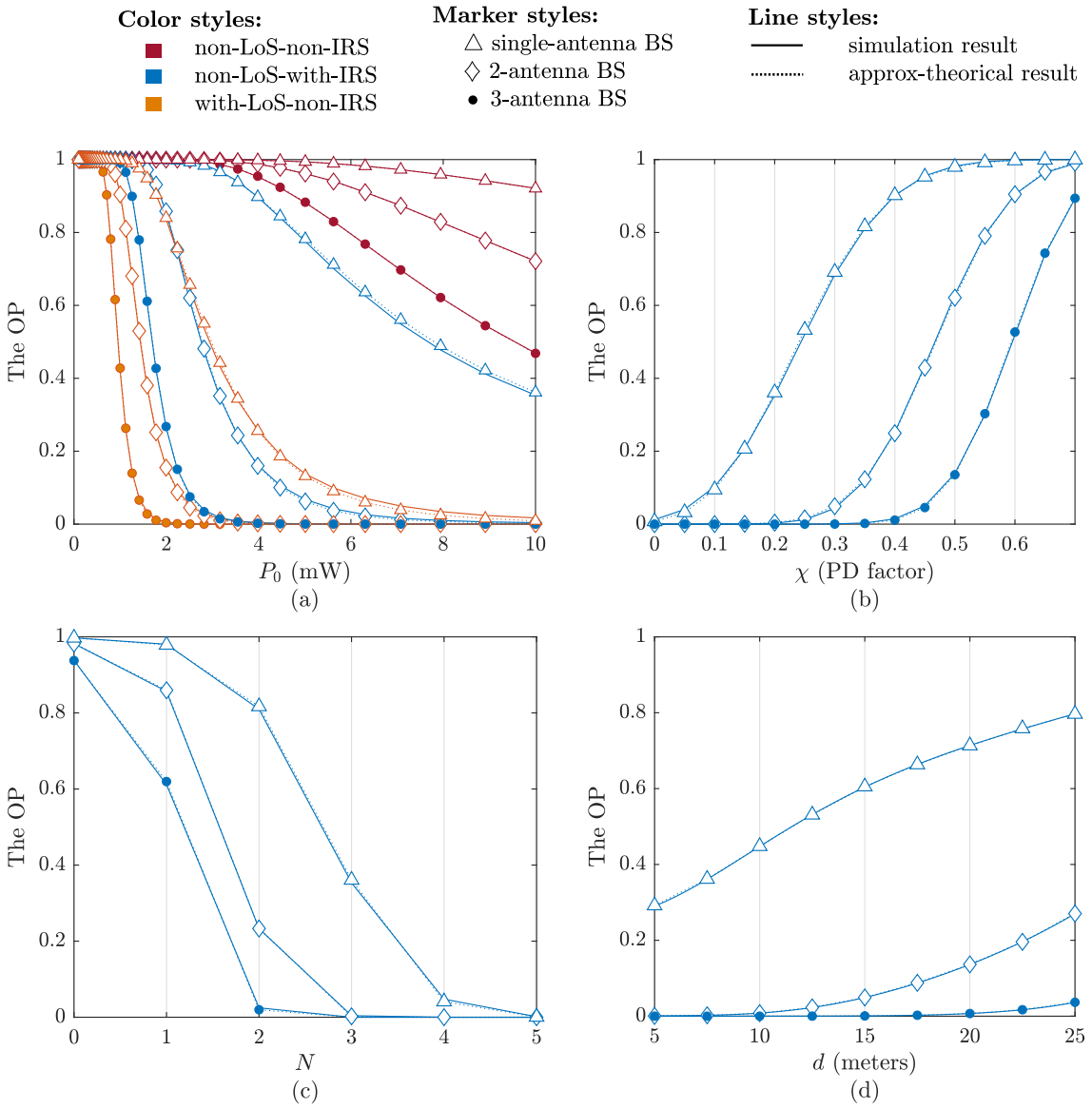

FIGURE 7. The effects of (a) the transmit power, (b) power distortion factor, (c) the number of the RTs and (d) the position of the IRS on the OP. The IRS's centre coordinate is $(d, 20)$ meters. Unless otherwise specified in the sub-figures, we set $P_0 = 10(mW)$, $\chi_n = 0.2, N = 3$.

key system parameters, such as the transmit power P_0, the distortion factor χ_n, the number of the RTs N, and the position of the IRS. The system setup is illustrated as in Fig. 4 and details of the simulation parameters is listed in Table 3. The OP and AR are optimized by applying the optimal weight vector $w(t) = \frac{h^{\dagger}_{Signal}(t)}{\|h_{Signal}(t)\|}$ at the BS (see the second paragraph of Section IV), adjusting the phase profile of each RT using (5), selecting the optimal Rx directivity using the rule given in the discussion of Fig. 6 and configuring the IRS's phase shifts as same as those in (27). Using these results, the accuracy of the proposed approximate distribution for the combined SNR can be evaluated. It is seen that the theoretical curves are very close their respective simulation curves. This indicates that our proposed approximate distribution is legitimate. Especially for the AR's results, the theoretical and the simulation curves are perfectly matched. For performance comparison, the three scenarios, i.e., with-LoS-non-IRS, non-LoS-with-IRS and non-LoS-non-IRS, are investigated. The results in Fig. 7(a) and 8(a) show the advantages of the IRS in enhancing the performance where the LoS link is not available. It can be realized that the performance for the non-LoS-non-IRS scenario is very poor as compared to the other scenarios. The distortion power gives a notable effect on the performance. For a fixed transmit power, the OP and the AR are respectively increasing functions (see Fig. 7(b)) and decreasing function (see Fig. 8(b)) of PD factor. Figs. 7(c) and 8(c) show the system performance for different values of N. Despite the presence of the distortion power, the signal-combining capability, which is obtained through adjusting the

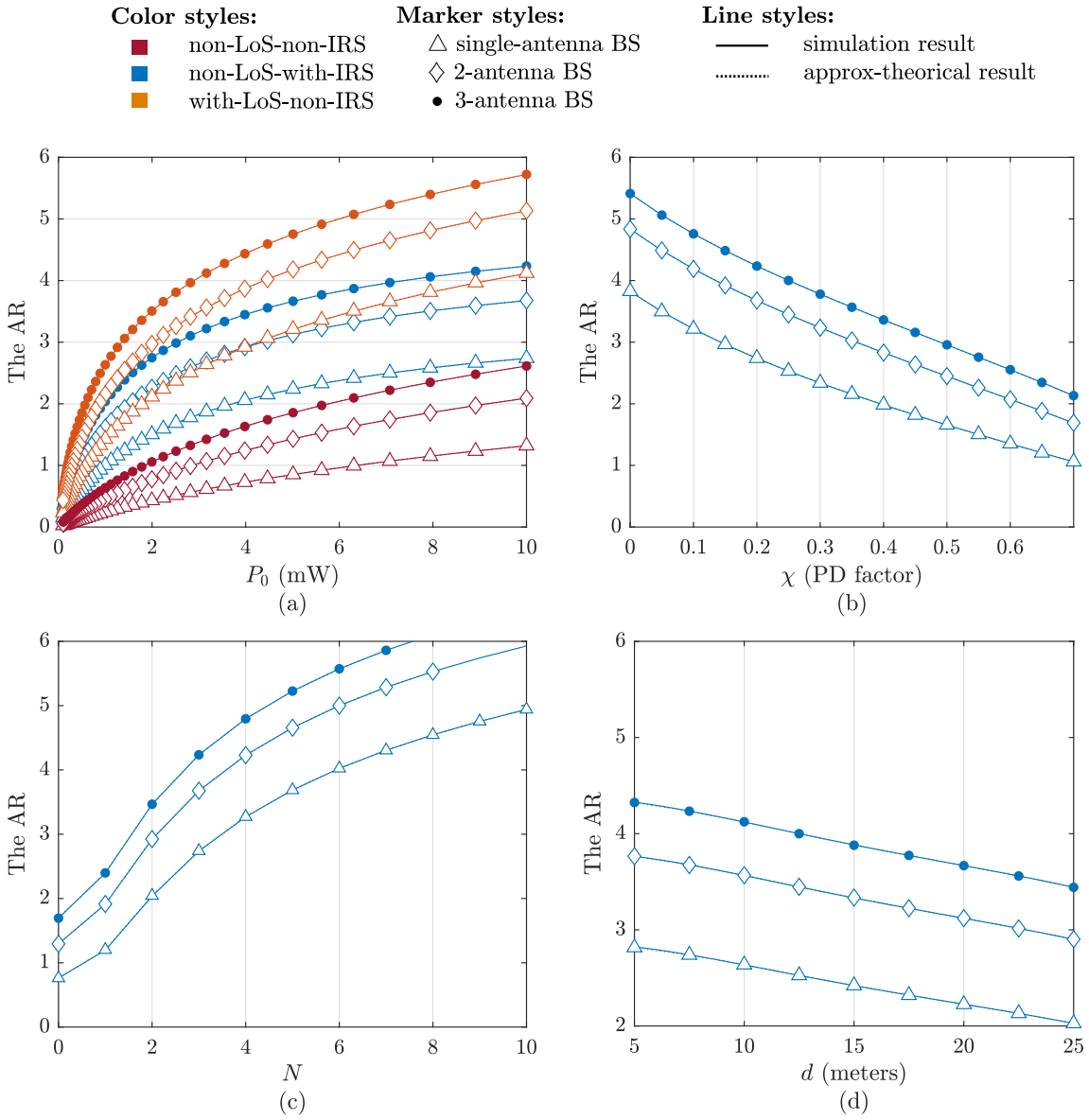

FIGURE 8. The effects of (a) the transmit power, (b) power distortion factor, (c) the number of the RTs and (d) the position of the IRS on the AR. The IRS's centre coordinate is $(d, 20)$ meters. Unless otherwise specified in the sub-figures, we set $P_0 = 10(mW)$, $\chi_n = 0.2, N = 3$.

phase shifts of the RTs, allows better performance when more RTs is utilized. Fig. 8(c) shows that the AR of the non-LoS-with-IRS scenario can overcome that of the with-LoS-non-IRS if N is sufficiently large (e.g., 7-RT IRS as shown in Fig. 8(c)). Figs. 7(d) and 8(d) show the influence of the IRS's position on the system performance. When the IRS moves close to the BS, a great amount of energy is captured within the area of the IRS and the IRS can compile more energy to the Rx antenna. Therefore, the IRS can sustain greater performance when it moves close to the BS and vice versa. However, in practical scenarios, if the IRS is too close to the BS, the far-field condition is not secured. This leads to major issues such as the infeasibility of the channel modelling task and the IRS's scalability.

V. CONCLUSION

In this paper, we proposed a novel channel model for IRSaWC using the physics characteristic of the reflection on the IRS and the modified SV model. We showed that the information signal at the receiver experiences a Rice fading. The theoretical results for the key parameters of the proposed channel, such as the K factor, the received information signal power, and the received distortion power, were derived. Especially, a gamma distribution-based approximate combined-SNR distribution was studied for facilitating the theoretical performance evaluation for IRSaMAWSs. The numerical results showed that the IRS is an efficient solution to enhance the system performance, especially when the LoS link is not available. Although the phase distortion occurring

from the RT's reflection gives an additional noise at the receiver, a higher number of the RTs can yield a higher performance with a reasonable phase-shift setup. Another advantage of the IRS is to provide a narrow reflection angle-beam, hence, providing good signal strengths at the desired positions and low interference to the overall network. A larger size of the RT allows a better signal strength and a narrower angle-beam. By adjusting the reflections on the RTs, the IRS is capable of manipulating the properties of the wireless environment; hence, our archived results are useful tools to develop efficient algorithms for boosting the performance of the IRSaWC.

APPENDIX A PROOF OF THE CALCULATIONS IN TABLE 2

In this section, we present the calculations for $\mathbb{C}_{3\text{GPP}}$ and $\mathbb{D}_{3\text{GPP}}$ given in Table 2. The values for $\mathbb{C}_{3\text{GPP}}$ and $\mathbb{D}_{3\text{GPP}}$ are calculated by using

$$\mathbb{E}\{G_{\{\text{Tx,Rx}\}}(x)\} = \int_{\theta_l-\Delta}^{\theta_l+\Delta} G_{\{\text{Tx,Rx}\}} p(x|\theta_l) dx. \tag{37}$$

A. FOR THE CASE OF $\theta_l \in [-\theta_c + \Delta, \theta_c - \Delta]$

Substituting the directivity model given in (12) and the probability density function given in (13), (37) in this case can be written as

$$\begin{aligned}
&\mathbb{E}\{G_{\{\text{Tx,Rx}\}}(x)\} \\
&= \frac{C_0}{\sigma\sqrt{2\pi}} \int_{\theta_l-\Delta}^{\theta_l+\Delta} \exp\left(-\frac{0.3\ln(10)}{\theta_{3\text{dB}}^2}x^2 - \frac{(x-\theta_l)^2}{2\sigma^2}\right) dx, \\
&= \frac{C_0 \exp\left(-\frac{0.3\ln(10)\theta_l^2}{0.6\ln(10)\sigma^2+\theta_{3\text{dB}}^2}\right)}{\sigma\sqrt{2\pi}} \int_{\theta_l-\Delta}^{\theta_l+\Delta} \\
&\quad \times \exp\left(-\frac{0.6\ln(10)\sigma^2+\theta_{3\text{dB}}^2}{2\sigma^2\theta_{3\text{dB}}^2}\right. \\
&\quad \left.\times \left(x - \frac{\theta_l}{\frac{0.6\ln(10)\sigma^2}{\theta_{3\text{dB}}}+1}\right)\right) dx, \\
&= \frac{C_0 \exp\left(-\frac{0.3\ln(10)\theta_l^2}{0.6\ln(10)\sigma^2+\theta_{3\text{dB}}^2}\right)}{\sqrt{2\pi}\sqrt{\frac{0.6\ln(10)\sigma^2}{\theta_{3\text{dB}}^2}+1}} \\
&\quad \times \int_{\frac{\theta_l}{\hat{\sigma}}\left(\frac{0.6\ln(10)\sigma^2}{0.6\ln(10)\sigma^2+\theta_{3\text{dB}}^2}\right)-\frac{\Delta}{\hat{\sigma}}}^{\frac{\theta_l}{\hat{\sigma}}\left(\frac{0.6\ln(10)\sigma^2}{0.6\ln(10)\sigma^2+\theta_{3\text{dB}}^2}\right)+\frac{\Delta}{\hat{\sigma}}} \exp\left(-\frac{t^2}{2}\right) dt.
\end{aligned} \tag{38}$$

where $t = x/\hat{\sigma}$.

After some manipulations, the expressions for $\mathbb{C}_{3\text{GPP}}$ and $\mathbb{D}_{3\text{GPP}}$ for the case of $\theta_l \in [-\theta_c + \Delta, \theta_c - \Delta]$can be obtained as in Table 2.

B. FOR THE CASE OF $\theta_l \in [-\theta_c - \Delta, -\theta_c + \Delta]$

In this case, the values of $\mathbb{C}_{3\text{GPP}}$ and $\mathbb{D}_{3\text{GPP}}$ is calculated as

$$\begin{aligned}
&\mathbb{E}\{G_{\{\text{Tx,Rx}\}}(x)\} \\
&= \int_{\theta_l-\Delta}^{\theta_l+\Delta} G_{\{\text{Tx,Rx}\}}(x)\, p(x|\theta_l) dx, \\
&= \underbrace{\frac{0.01C_0}{\sigma\sqrt{2\pi}} \int_{\theta_l-\Delta}^{-\theta_c} \exp\left(-\frac{(x-\theta_l)^2}{2\sigma^2}\right) dx}_{\mathcal{I}_1} \\
&\quad + \underbrace{\frac{C_0}{\sigma\sqrt{2\pi}} \int_{-\theta_c}^{\theta_l+\Delta} \exp\left(-\frac{0.3\ln(10)}{\theta_{3\text{dB}}^2}x^2 - \frac{(x-\theta_l)^2}{2\sigma^2}\right) dx}_{\mathcal{I}_2}.
\end{aligned} \tag{39}$$

Letting $t = \frac{x-\theta_l}{\sigma}$, $\mathcal{I}_1$ is calculated as

$$\begin{aligned}
\mathcal{I}_1 &= \frac{0.01\ C_0}{\sqrt{2\pi}} \int_{-\frac{\Delta}{\sigma}}^{-\frac{\theta_c+\theta_l}{\sigma}} \exp\left(-\frac{t^2}{2}\right) dt, \\
&= 0.01\ C_0 \left(\Phi\left(-\frac{\theta_c+\theta_l}{\sigma}\right) - \Phi\left(-\frac{\Delta}{\sigma}\right)\right).
\end{aligned} \tag{40}$$

Following similar steps as in Appendix V-A, $\mathcal{I}_2$ is calculated as

$$\begin{aligned}
I_2 &= \frac{C_0 \exp\left(-\frac{0.3\ln(10)\theta_l^2}{0.6\ln(10)\sigma^2+\theta_{3\text{dB}}^2}\right)}{\sqrt{2\pi}\sqrt{\frac{0.6\ln(10)\sigma^2}{\theta_{3\text{dB}}^2}+1}} \\
&\quad \times \int_{-\frac{\theta_c}{\hat{\sigma}}-\frac{\theta_l}{\hat{\sigma}}\frac{\theta_{3\text{dB}}^2}{0.6\ln(10)\sigma^2+\theta_{3\text{dB}}^2}}^{\frac{\theta_l}{\hat{\sigma}}\left(\frac{0.6\ln(10)\sigma^2}{0.6\ln(10)\sigma^2+\phi_{3\text{dB}}^2}\right)+\frac{\Delta}{\hat{\sigma}}} \exp\left(-\frac{t^2}{2}\right) dt, \\
&= \frac{C_0 \exp\left(-\frac{0.3\ln(10)\theta_l^2}{0.6\ln(10)\sigma^2+\theta_{3\text{dB}}^2}\right)}{\sqrt{\frac{0.6\ln(10)\sigma^2}{\theta_{3\text{dB}}^2}+1}} \\
&\quad \times \left(\begin{array}{l}\Phi\left(\frac{\theta_l}{\hat{\sigma}}\left(\frac{0.6\ln(10)\sigma^2}{0.6\ln(10)\sigma^2+\theta_{3\text{dB}}^2}\right)+\frac{\Delta}{\hat{\sigma}}\right) \\ -\Phi\left(-\frac{\theta_c}{\hat{\sigma}}-\frac{\theta_l}{\hat{\sigma}}\frac{\theta_{3\text{dB}}^2}{0.6\ln(10)\sigma^2+\theta_{3\text{dB}}^2}\right)\end{array}\right).
\end{aligned} \tag{41}$$

Using (40) and (41), the expressions for $\mathbb{C}_{3\text{GPP}}$ and $\mathbb{D}_{3\text{GPP}}$ for the case of $\theta_l \in [-\theta_c - \Delta, -\theta_c + \Delta]$ can be obtained as in Table 2.

C. FOR THE CASE OF $\theta_l \in [\theta_c - \Delta, \theta_c + \Delta]$

In this case, the values of $\mathbb{C}_{3\text{GPP}}$ and $\mathbb{D}_{3\text{GPP}}$ is calculated as

$$\begin{aligned}
\mathbb{E}\{G_{\{\text{Tx,Rx}\}}(x)\} &= \int_{\theta_l-\Delta}^{\theta_l+\Delta} G_{\{\text{Tx,Rx}\}}(x)\, p(x|\theta_l) dx, \\
&= \frac{C_0}{\sigma\sqrt{2\pi}} \int_{\theta_l-\Delta}^{\theta_c} \\
&\quad \times \exp\left(-\frac{0.3\ln(10)}{\theta_{3\text{dB}}^2}x^2 - \frac{(x-\theta_l)^2}{2\sigma^2}\right) dx \\
&\quad + \frac{0.01C_0}{\sigma\sqrt{2\pi}} \int_{\theta_c}^{\theta_l+\Delta} \exp\left(-\frac{(x-\theta_l)^2}{2\sigma^2}\right) dx.
\end{aligned} \tag{42}$$

Following similar steps as in Appendix V-B, the expressions for $\mathbb{C}_{3GPP}$ and $\mathbb{D}_{3GPP}$ for the case of $\theta_l \in [\theta_c - \Delta, \theta_c + \Delta]$ can be obtained as in Table 2.

D. FOR THE REMAIN VALUES OF θ_l

In this case, the values of $\mathbb{C}_{3GPP}$ and $\mathbb{D}_{3GPP}$ is calculated as

$$\mathbb{E}\{G_{\{\text{Tx,Rx}\}}(x)\} = \int_{\theta_l-\Delta}^{\theta_l+\Delta} 0.01\, p(x|\phi_l)dx = 0.01. \quad (43)$$

REFERENCES

[1] J. Zhang, H. Du, Q. Sun, B. Ai, and D. W. K. Ng, "Physical layer security enhancement with reconfigurable intelligent surface-aided networks," *IEEE Trans. Inf. Forensics Security*, vol. 16, pp. 3480–3495, 2021.

[2] Q. Wu and R. Zhang, "Intelligent reflecting surface enhanced wireless network via joint active and passive beamforming," *IEEE Trans. Wireless Commun.*, vol. 18, no. 11, pp. 5394–5409, Nov. 2019.

[3] C. Cao, Z. Lian, Y. Wang, Y. Su, and B. Jin, "A non-stationary geometry-based channel model for IRS-assisted UAV-MIMO channels," *IEEE Commun. Lett.*, vol. 25, no. 12, pp. 3760–3764, Dec. 2021.

[4] H. Jiang, C. Ruan, Z. Zhang, J. Dang, L. Wu, M. Mukherjee, and D. B. D. Costa, "A general wideband non-stationary stochastic channel model for intelligent reflecting surface-assisted MIMO communications," *IEEE Trans. Wireless Commun.*, vol. 20, no. 8, pp. 5314–5328, Aug. 2021.

[5] H. Jiang, Z. Zhang, C.-X. Wang, J. Zhang, J. Dang, L. Wu, and H. Zhang, "A novel 3D UAV channel model for A2G communication environments using AoD and AoA estimation algorithms," *IEEE Trans. Commun.*, vol. 68, no. 11, pp. 7232–7246, Nov. 2020.

[6] M. Zeng, X. Li, G. Li, W. Hao, and O. A. Dobre, "Sum rate maximization for IRS-assisted uplink NOMA," *IEEE Commun. Lett.*, vol. 25, no. 1, pp. 234–238, Jan. 2021.

[7] Q. Wu and R. Zhang, "Weighted sum power maximization for intelligent reflecting surface aided SWIPT," *IEEE Wireless Commun. Lett.*, vol. 9, no. 5, pp. 586–590, May 2020.

[8] T. Hou, Y. Liu, Z. Song, X. Sun, Y. Chen, and L. Hanzo, "MIMO assisted networks relying on intelligent reflective surfaces," 2019, *arXiv:1910.00959*.

[9] J. Chen, Y.-C. Liang, Y. Pei, and H. Guo, "Intelligent reflecting surface: A programmable wireless environment for physical layer security," *IEEE Access*, vol. 7, pp. 82599–82612, 2019.

[10] K. Feng, X. Li, Y. Han, S. Jin, and Y. Chen, "Physical layer security enhancement exploiting intelligent reflecting surface," *IEEE Commun. Lett.*, vol. 25, no. 3, pp. 734–738, Mar. 2021.

[11] V. P. Tuan and I. P. Hong, "Secrecy performance analysis and optimization of intelligent reflecting surface-aided indoor wireless communications," *IEEE Access*, vol. 8, pp. 109440–109452, 2020.

[12] C. Liaskos, S. Nie, A. Tsioliaridou, A. Pitsillides, S. Ioannidis, and I. Akyildiz, "Realizing wireless communication through software-defined HyperSurface environments," in *Proc. IEEE 19th Int. Symp. World Wireless, Mobile Multimedia Networks (WoWMoM)*, Jun. 2018, pp. 14–15.

[13] C. Liaskos, S. Nie, A. Tsioliaridou, A. Pitsillides, S. Ioannidis, and I. Akyildiz, "A novel communication paradigm for high capacity and security via programmable indoor wireless environments in next generation wireless systems," *Ad Hoc Netw.*, vol. 87, pp. 1–16, May 2019.

[14] Y. Wei, M.-M. Zhao, and M.-J. Zhao, "Channel distribution learning: Model-driven GAN-based channel modeling for IRS-aided wireless communication," *IEEE Trans. Commun.*, vol. 70, no. 7, pp. 4482–4497, Jul. 2022.

[15] O. Özdogan, E. Björnson, and E. G. Larsson, "Intelligent reflecting surfaces: Physics, propagation, and pathloss modeling," *IEEE Wireless Commun. Lett.*, vol. 9, no. 5, pp. 581–585, May 2020.

[16] S. Mukherjee, S. S. Das, A. Chatterjee, and S. Chatterjee, "Analytical calculation of Rician K-factor for indoor wireless channel models," *IEEE Access*, vol. 5, pp. 19194–19212, 2017.

[17] I. S. Gradshteyn, I. M. Ryzhik, A. Jeffrey, and D. Zwillinger, *Table of Integral, Series and Products*, 7th ed. Amsterdam, The Netherlands: Elsevier, 2007.

[18] C. A. Balanis, *Advanced Engineering Electromagnetics*, 2nd ed. Hoboken, NJ, USA: Wiley, 2012.

[19] SCM. *Spatial Channel Model Text Description—V4.2B*, document SCM-132, 3GPP, Apr. 2003.

[20] A. A. M. Saleh and R. Valenzulea, "A statistical model for indoor multipath propagation," *IEEE J. Sel. Areas Commun.*, vol. SAC-5, no. 2, pp. 128–137, Feb. 1987.

[21] M. K. Arti and M. R. Bhatnagar, "Maximal ratio transmission in AF MIMO relay systems over Nakagami-*m* fading channels," *IEEE Trans. Veh. Tech.*, vol. 64, no. 5, pp. 1895–1903, May 2015.

[22] L.-C. Wang and C.-T. Lea, "Co-channel interference analysis of shadowed Rician channels," *IEEE Commun. Lett.*, vol. 2, no. 3, pp. 67–69, Mar. 1998.

[23] P. Ju, W. Song, and A.-L. Jin, "Exact outage probability for a wireless diversity network with spatially random mobile relays," *IEEE Commun. Lett.*, vol. 18, no. 9, pp. 1641–1644, Sep. 2014.

[24] V. P. Tuan and I.-P. Hong, "Enhancing secrecy performance for NOMA systems with intelligent reflecting surface: Analysis and optimization," *IEEE Access*, vol. 9, pp. 99060–99072, 2021.

VAN PHU TUAN received the B.E. and M.E. degrees in electronics and telecommunications engineering from the Ho Chi Minh City University of Technology (HCMUT), Vietnam, in 2010 and 2013, respectively, and the Ph.D. degree in electrical engineering from the University of Ulsan (UOU), Ulsan, South Korea, in 2018. From 2018 to 2019 and from 2019 to 2021, he was a Postdoctoral Researcher at the UOU and Kongju National University (KNU), Cheonan, South Korea, respectively. He is currently with Dong-A University (UDA), Da Nang, Vietnam. His major research interests include wireless communications systems, physical layer security, wireless powered communications, IRS-aided wireless communication, machine learning, and optimization methods.

IC PYO HONG (Member, IEEE) received the B.S., M.S., and Ph.D. degrees in electronics engineering from Yonsei University, Seoul, South Korea, in 1994, 1996, and 2000, respectively. From 2000 to 2003, he was at the Information and Communication Division, Samsung Electronics Company, Suwon, South Korea, where he was a Senior Engineer with CDMA Mobile Research. He was a Visiting Scholar with Texas A&M University, College Station, TX, USA, in 2006, and Syracuse University, Syracuse, NY, USA, in 2012. Since 2003, he has been with the Department of Information and Communication Engineering, Kongju National University, Cheonan, South Korea, where he is currently a Professor. His research interests include numerical techniques in electromagnetics and periodic electromagnetic structures.